J. Fluid Mech. (1995), *vol.* 294, *pp.* 323–347

Thermocapillary flow with evaporation and condensation at low gravity. Part 1. Non-deforming surface

By G. R. SCHMIDT[1], T. J. CHUNG[2] AND A. NADARAJAH[3]

[1] Propulsion Laboratory, NASA Marshall Space Flight Center, Huntsville, AL 35812, USA

[2] Department of Mechanical Engineering, University of Alabama in Huntsville, Huntsville, AL 35899, USA

[3] Department of Chemical Engineering, University of Alabama in Huntsville, Huntsville, AL 35899, USA

(Received 30 July 1992 and in revised form 2 February 1995)

The problem of steady motion and thermal behaviour of a volatile, wetting liquid in an open cavity under low gravity is defined and examined. The domain geometrically approximates a two-phase pore of liquid on a wicking structure surface, and consists of a 1 to 10^2 μm wide rectangular cavity bounded by a saturated vapour and liquid reservoir on its upper and lower surfaces, respectively. Thermal non-equilibrium and convection are established by symmetrically superheating or subcooling the pore boundaries by ~ 1 K relative to the vapour. Numerical analyses show that although thermocapillary flow competes with interfacial phase change in dictating the circulation and flow structure, it tends to reinforce the convective effects of evaporation and condensation on surface temperature and heat transport. In addition, highly wetting fluids with curved menisci are characterized by greater circulation intensities and dynamic pressure gradients than a flat surface. The magnitude of these gradients suggests that the fixed menisci shapes assumed in this study are unrealistic, and that the influence of convection on surface morphology should be considered.

1. Introduction

Understanding the nature of two-phase convection near the surfaces of liquid-filled wicking structures and porous media is important to the design of many engineering systems. Example applications include heat pipes, capillary pumped loops, spacecraft liquid acquisition devices and passive cryogenic pressure control systems. In most cases, the wicking structure surface is exposed to a vapour or vapour/gas mixture, and consists of numerous cavities connected to a channel, reservoir or porous internal region. Thermal non-equilibrium between the liquid, vapour and structure drives several convection modes within these surface pores. The most notable one is thermocapillary flow which arises from thermally induced surface tension variation along the meniscus. Two other modes that become important when the liquid is close to a saturated state are evaporation and condensation. All three of these can greatly influence heat transfer and performance by causing a departure from the basic-state interfacial temperature distribution and altering the morphology of the free surface. The latter effect can be particularly detrimental in applications where a pressure differential is maintained across the liquid/gas interface, such as low-gravity fluid acquisition devices and passive pressure control systems. Surface deformation in these cases can lead to loss of mechanical equilibrium and degradation in liquid retention capability.

Although the influence of combined two-phase thermocapillary flow on liquid retention has never been theoretically assessed, the individual convection modes associated with this problem have been examined separately for numerous applications. Most prior work involving thermocapillarity and the closely related topic of combined thermocapillary–buoyancy-driven flow has been done in the area of materials processing (Ostrach & Kamotani 1992). A popular geometry for the study of pure and combined convection is the rectangular cavity with isothermal sidewalls and a horizontal upper free surface. Numerical investigations by Bergman & Ramadhyani (1986), Bergman & Keller (1988), Jue, Ramaswamy & Akin (1991), and Hadid & Roux (1992) yielded insight into the sensitivity of flow variables to key dimensionless parameters. Several researchers have applied the same geometry to evaluate thermocapillary convection with a deformable liquid surface. Sen & Davis (1982), Sen (1986) and Strani, Piva & Graziani (1983) applied asymptotic methods to determine the flow field and free surface shape at the ends and core of differentially heated slots, while Zebib, Homsy & Meiberg (1985) and Carpenter & Homsy (1989) examined the effect of interface geometry by means of perturbation techniques. Cylindrical geometries have also been used to investigate thermocapillary- and buoyancy-driven flow in melt regions. Earlier studies by Fu & Ostrach (1983), Shen *et al.* (1990), and Kobayashi (1988) assumed a fixed surface independent of convective effects. Somewhat more recently, Duranceau & Brown (1989), Hyer, Jankowski & Neitzel (1991) and Lan & Kou (1991) addressed the problem of a cylindrical float zone with a deformable interface. They applied a pinning condition at the contact point and observed little flow-induced deformation.

In all cases the variation of free surface geometry due to thermocapillarity was treated as a lower-order effect. It was usually neglected by assuming a small thermal variation of surface tension with respect to a reference (i.e. low crispation number Cr) and low ratio of viscous to surface tension forces (i.e. low capillary number Ca). In combined thermocapillary–buoyancy-driven flows the deformation under terrestrial gravity was caused by hydrostatic effects, while the surface remained essentially flat in a microgravity environment. These results and the assumption of vanishingly small Ca and Cr were entirely consistent with the relatively large domains considered in these studies. However, in an analysis of pure thermocapillary flow, Sen (1986) applied an independent coupling of the meniscus force balance condition to show that the interface can undergo significant deflections with large values of Cr. Assuming a prescribed contact angle, Cuvelier & Driessen (1986) found that the free boundary is highly sensitive to Ca. Furthermore, Kamotani & Platt (1992) recently showed that variation in surface geometry could greatly influence convection within the cavity for thermocapillary–buoyancy-driven flow. Through experiments and numerical analysis, they compared the convection and heat transfer characteristics of a flat and curved 10°-contact angle surface, and noted a marked reduction in thermocapillarity, flow intensity and local heat transfer rate with the highly curved surface.

The small cavities associated with wicking structures and retention devices present a situation where surface tension forces are dominant with relatively large values of Ca and Cr. In such instances, the surface deformation arising from thermocapillarity may be significant and could affect the flow field and heat transfer in a variety of ways. Thus, results from the above investigations have only marginal application to the study of convection on the surfaces of porous structures.

Evaporation and condensation add yet another degree of complexity to this problem. Most prior studies of evaporating and condensing menisci have focused on either the intrinsic meniscus or the submicron region near the interline where the solid substrate plays an important role in surface phenomena. Examinations of the submicron region have concentrated on the behaviour of thin liquid films and menisci close to solid surfaces. Here, buoyancy and convective terms in the momentum equation are typically ignored, and the relationship between thermocapillary stress and liquid/solid intermolecular forces is emphasized (Potash & Wayner 1972; Renk & Wayner 1979; Werhle & Voulelikas 1985; Mirsamoghadam & Catton 1988). In a study of evaporating and condensing film stability, Burelbach, Bankoff & Davis (1988) treated the van der Waals forces as a body force term and noted that the combined action of this attraction, thermocapillarity and interfacial flow could lead to significant instability and deformation of the surface. This behaviour was also observed in several other references cited by Burelbach *et al.* Recently, Swanson & Herdt (1992) and Swanson & Peterson (1993) modelled the complete meniscus by matching solutions in the interline and intrinsic regions.

It should be clear from the above discussions that the dominance of surface tension forces, coupled with interfacial phase change, makes the fluid retention problem quite different from others. This uniqueness is accentuated by the very small contact angles encountered in fluid retention systems (as compared with contact angles $\sim 90°$ for melts in materials processing) and by the mass transfer with liquid in the porous structure. A situation very similar to this problem was examined by Chen, Oshima & Hinada (1989) who assessed a one-sided model of a superheated wetting liquid in a square cavity with isothermal sidewalls. Like other researchers, they ignored the influence of convection on surface morphology. Although a competition between thermocapillarity and evaporation in dictating flow structure was observed, they did not provide a firm explanation of this phenomenon or consider the related aspect of condensation. In addition, by resorting to a streamfunction–vorticity formulation, they failed to recognize the dramatic influence of small contact angles and thermocapillary flow on interfacial pressure and surface morphology.

The limited applicability of prior studies and unique features of retention phenomena warrant an original definition and thorough investigation of this unfamiliar problem. Although we are primarily concerned with determining if thermocapillarity and mass transfer can lead to large variations in surface morphology, given the complexity of the problem and the large number of variables involved it is necessary to first understand the nature of velocity, pressure and temperature distributions within the pore domain. This can be best accomplished by examining the steady-state flow field about a fixed circular surface. Such a domain will be examined in this paper, but we will adopt an approach that provides a basis for studying the more complex problem of a deforming surface in part 2 (Schmidt, Chung & Nadarajah 1995). In the next section, the mathematical model appropriate for a non-deforming pore domain will be developed, while in §3 scaling analyses will be performed to simplify these equations and assess the importance of various terms in the boundary conditions. Following a brief summary of the numerical method used to solve the defining equations in §4, the results of numerical simulations will be presented and discussed in §5.

2. Theoretical model

The solid substrate of a typical porous structure usually consists of a complex interweave of metal wires or random arrangement of sintered metallic fragments. Basing an assessment on an actual application would be very difficult owing to the extreme variability in contact surface geometry and uncertainty regarding interior flow conditions. To avoid this issue, we consider the domain shown in figure 1 which represents a greatly simplified rendition of a single pore, but still permits taking into account key meniscus transport phenomena. The domain consists of a two-dimensional rectangular groove partially filled with an incompressible Newtonian liquid. The cavity is assumed to be oriented with respect to a uniform downward-pointing acceleration field. The left and right sides of the pore (boundaries 1 and 3, respectively) consist of solid vertical sidewalls at temperature T_1. The lower boundary 2, which is also at temperature T_1, opens to a large reservoir of liquid to enable balancing of mass flow through the cavity. The upper surface (boundary 4) is represented by a circular meniscus $y^{(s)}$ which is symmetric about the pore centreline. This interface is bounded by an inert vapour which is at saturation temperature T_0 far from the interface. The meniscus is assumed to wet the solid sidewalls at an acute contact angle ω, and is further characterized by the unit normal and tangent vectors n_i and s_i and contour angle α. The temperature difference T_1-T_0 drives all fluid flow and heat transfer within the cavity.

Considering a fixed circular surface is equivalent to assuming a gravity-free environment and ignoring pressure, vapour recoil and viscous stress terms in the normal jump momentum balance for the meniscus. Under terrestrial conditions, this assumption is probably inappropriate, since the length scales at which surface tension dominates over thermocapillarity and viscosity ($D \geqslant 10^2$ μm) yield increasing contributions from hydrostatic pressure and buoyancy. However, in microgravity with moderate pore dimensions, we can expect to find instances where such an assumption is valid. Another important assumption is the neglect of intermolecular forces between liquid and solid. For the geometry and dimensional range of this problem, intermolecular attraction between the liquid and solid is best accounted for by a contact angle constraint rather than a corrected surface or body force. The scaled governing equations for the fluid in the cavity, with the Boussinesq approximation, are expressed as

$$V_{i,i} = 0, \tag{1}$$

$$\frac{\partial V_i}{\partial t} + V_j V_{i,j} + P_{,i} - V_{i,jj} - Gr\, a_i T = 0, \tag{2}$$

$$\frac{\partial T}{\partial t} + V_j T_{,j} - \frac{1}{Pr} T_{,jj} = 0. \tag{3}$$

Although only steady-state solutions will be considered in this study, the transient terms are included in the problem definition since they are used to obtain the numerical steady-state solution. Here, V_i is the fluid velocity; T is the temperature; P is the dynamic pressure; and a_i is the unit vector in the direction of the imposed gravitational acceleration. The variables describing this problem are scaled on the pore width D and the viscous time scale D^2/ν, where ν is the kinematic viscosity. For temperature, we scale the difference between the liquid and vapour temperatures by $|\Delta T| = |T_1-T_0|$, where T_1 and T_0 are the sidewall and vapour temperatures, respectively. The scaled vapour temperature conveniently assumes the same value of 0 for both superheating and subcooling. With superheating the sidewall temperature is fixed at $T = 1$, while with subcooling, it is held at $T = -1$. Apart from the linear temperature dependence applied to density ρ and surface tension γ, all thermophysical properties are treated as constant. Here γ and ρ are referenced at the minimum domain temperature which is

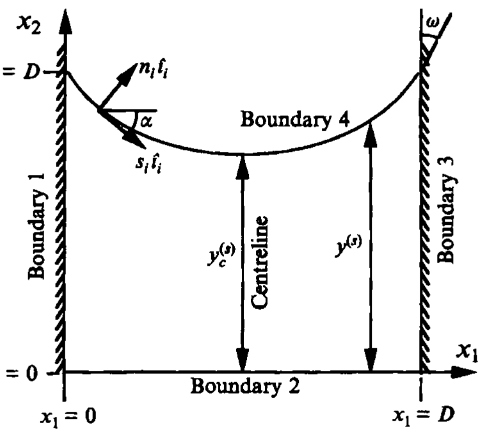

FIGURE 1. Problem domain.

T_0 for superheating and T_1 for subcooling. The dimensionless parameters arising from the scaling are the Grashoff number *Gr* and Prandtl number *Pr*, defined as

$$Gr = D^3 g\beta|\Delta T|/(\nu^2), \tag{4}$$

$$Pr = \nu/\zeta \tag{5}$$

where β and ζ are the thermal expansivity and diffusivity, respectively.

The unique aspects of this problem are embodied in the boundary conditions applied at the sidewalls, reservoir interface and meniscus surface. Both of the sidewalls are assumed to be isothermal and are held at $T = 1$ and -1 for superheating and subcooling, respectively. We also assume impermeability and no-slip to yield the velocity condition $V_t = 0$.

On boundary 2, we apply the same temperature condition as the sidewall, that is $T = \pm 1$. We also assume that the flow into and out of the cavity is parallel and uniform. Consequently, $V_1 = 0$, and the average flux required to balance the total flow across boundary 4 is applied uniformly as the V_2 boundary condition. From an overall pore mass balance we obtain

$$V_2 = \frac{1}{\Gamma_2}\int_{\Gamma_4} \frac{T}{Rs}\,\mathrm{d}\Gamma_4. \tag{6}$$

Γ_2 and Γ_4 are the areas of boundaries 2 and 4, respectively. *Rs* defines the degree of non-equilibrium (i.e. difference in state between the liquid and vapour) that can be maintained per unit mass undergoing phase change at a volatile interface. It relates mass flux j to the interfacial temperature jump according to $j = T/Rs$ and is derived by applying equilibrium thermodynamic assumptions to the Hertz–Knudsen equation on boundary 4 (Palmer 1976):

$$Rs = \frac{f_\rho \nu T_0^{3/2}}{eDL|\Delta T|}\left(\frac{2\pi R_g}{M_W}\right)^{1/2}. \tag{7}$$

Here, e is the accommodation coefficient and represents the resistance to mass transfer. For a surface free from contaminants, $e = 1$. Other variables in (7) include the ratio of liquid to vapour density f_ρ, latent heat L, vapour molecular weight M_W and universal gas constant R_g. $Rs = 0$ corresponds to the equilibrium limit, where the interfacial temperature is constant and equal to the saturation value, $T = 0$. $1/Rs = 0$ corresponds to the non-volatile case in which $j = 0$.

The velocity conditions on boundary 4 are obtained from the tangential jump momentum and jump mass balances. For the tangential balance, we apply the one-sided approximation and ignore vapour viscous stress to yield

$$\tau_{ij} n_j = -\frac{Ma}{Pr} T_{,i}, \tag{8}$$

where the scaled viscous stress tensor is defined as $\tau_{ij} = (V_{i,j} + V_{j,i})$, and the Marangoni number Ma is

$$Ma = \frac{|\partial \gamma / \partial T| D |\Delta T|}{\rho \nu \zeta}. \tag{9}$$

The normal gradients of V_1 and V_2 are interdependent and mutually satisfied by applying the Neumann condition in (8) to either velocity component. By applying (8) to V_1, we can use the equation for local mass flux as the condition for V_2, namely

$$V_2 = \frac{1}{n_2}\left(\frac{T}{Rs} - V_1 n_1\right). \tag{10}$$

For temperature on boundary 4, we take into account the heat transfer due to convective motion of the vapour relative to the liquid, latent heat transport and kinetic energy transport. When all these effects are included, the scaled energy equation becomes

$$T_{,i} n_i - f_k T_{,i}^{(v)} n_i = -(Bi_c + Bi_m + Bi_{ke} T^2)\, T, \tag{11}$$

where $T_{,i}^{(v)}$ is the temperature gradient in the vapour at the interface, and f_k is the ratio of vapour to liquid thermal conductivity. Bi_c, Bi_m and $Bi_{ke} T^2$ are the so-called convective, mass transfer and kinetic energy Biot numbers, respectively and are defined as

$$Bi_c = hD/k, \tag{12}$$

$$Bi_m = 1/(RsE), \tag{13}$$

$$Bi_{ke} = (f_\rho^2 - 1)\, \nu^3 \rho / (2D^2 k |\Delta T| Rs^3). \tag{14}$$

The parameter E has been termed the evaporation number by Burelbach *et al.* (1988) and is given by

$$E = k|\Delta T| / (\rho \nu L). \tag{15}$$

E represents the ratio between the viscous and evaporation/condensation time scales (i.e. D^2/ν and $\rho D^2 L/(k|\Delta T|)$, respectively) and is indicative of the rate of phase change relative to momentum diffusion in the cavity. A large value of E signifies a high rate of evaporation or condensation and shorter time scale relative to viscous effects. By applying the one-sided assumption (i.e. $f_k \rightarrow 0$) and combining the Biot numbers defined in (12)–(14) into a single term Bi, we can express the energy jump balance in a form equivalent to Newton's law of cooling, that is

$$T_{,i} n_i = -Bi\, T. \tag{16}$$

Equations (1)–(16) completely define the problem and will be used to obtain the steady-state fluid flow and temperature fields.

3. Scaling analysis

To make the numerical investigations physically relevant, we first ascertain via parametrics the magnitude and sensitivity of the principal dimensionless groupings identified in §2 over a range of thermophysical properties, pore widths D and

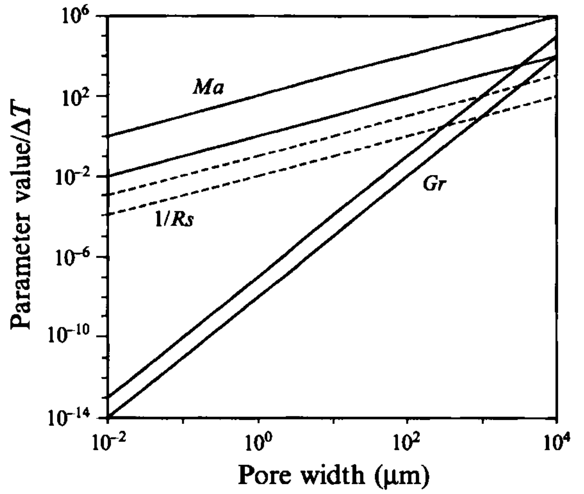

FIGURE 2. Sensitivity of dimensionless parameters associated with solution of V_i and P: upper and lower bounds.

superheating/subcooling limits $|\Delta T|$. Using the thermophysical properties of water, ethanol, Refrigerant-114 and ammonia as a reference, a modified parameter value, in which D and $|\Delta T|$ are factored out, is calculated for each fluid and used to estimate parameter bounds at different values of D and $|\Delta T|$.

To evaluate sensitivity to pore size, we consider a range of D from 10^{-2} to 10^4 µm. Although 1 µm represents a reasonable lower limit for most fine mesh screens, porous surfaces and wicking structures, we select 10^{-2} µm to broaden the range of study. In addition, 10^{-2} µm generally represents the upper limit at which long-range intermolecular forces between the liquid and solid begin to influence surface morphology. The upper bound of D, 10^4 µm ($= 1$ cm), is arbitrarily defined as a maximum, since characteristic dimensions in which $D \geqslant 10^5$ µm ($= 10$ cm) fall more in the category of a small container and out of the size range of this study. The maximum superheat ΔT that can be sustained without causing nucleation depends on the fluid, contact surface roughness and pore width. For the size range considered here, a bound of 10^{-1} to 1 K seems reasonable. However, to emphasize the effect of larger superheats, which are encountered with thin films, an upper limit of 10 K is assumed.

Solution of velocity and dynamic pressure requires the parameters in (2), (8) and (10). Fixing $Pr = 1$, the sensitivities of Gr, Ma and $1/Rs$ to D and ΔT are shown in figure 2. Note that these groupings exhibit the same proportional functional dependence on ΔT. We find that the different functional behaviours of Ma and Gr on D divide the velocity solution into three types of regimes. The thermocapillary regime occurs at $D < 10^3$ µm where $Ma \gg Gr$. In this region, velocity is dictated by surface tension variation and to a comparable extent the sensitivity of $1/Rs$ to temperature. The influence of Gr is essentially non-existent.

Extrapolating the trends in figure 2 to larger pore widths indicates that the regime where buoyancy forces dominate over thermocapillary and evaporative effects occurs at $D > 10^5$ µm). Between this point and the upper limit for pure thermocapillary flow ($D \sim 10^3$ µm), there exists a regime where buoyancy and thermocapillary forces compete. Here, the forces can either augment or offset each other depending on the orientation of the acceleration field and locations of applied heating and cooling.

The complete temperature solution primarily involves the boundary condition (16).

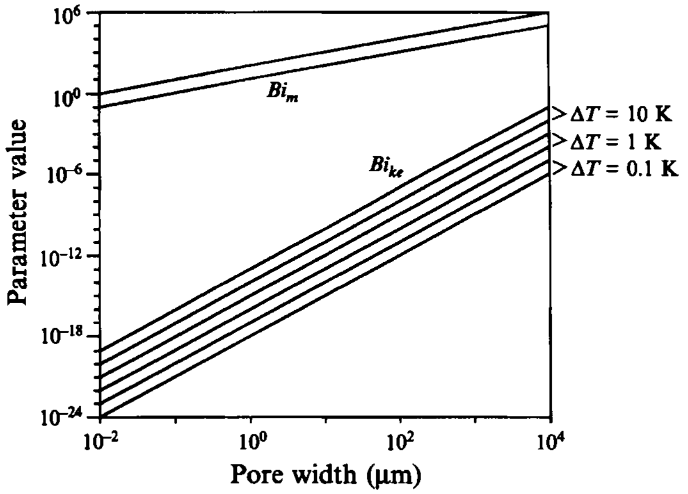

FIGURE 3. Sensitivity of dimensionless parameters associated with solution of T.

The relative sensitivity of the two variables arising from (16), Bi_m and Bi_{ke}, is shown in figure 3. Bi_m increases linearly with D from 10 at $D = 1$ μm, to 10^6 at $D = 10^4$ μm. Although Bi_{ke} varies linearly with D^2 and ΔT, its magnitude is so low that it never contributes to interfacial temperature. The trend in figure 3 suggests that it may become important only at characteristic dimensions significantly greater than the upper limit of this study.

In summary, we see that Gr and Bi_{ke} are vanishingly small in the size range considered here and can be ignored in this problem. The key parameters needed for solution of velocity are Ma, Rs and Bi which are in the ranges: $10^{-1} < Ma < 10^3$, $10^{-1} < Rs < 10^3$ and $1 < Bi < 10^4$.

4. Numerical model

A detailed description of the numerical model is given by Schmidt (1993) and only its key features will be summarized here. The finite element method was selected mainly because of its strength in handling unstructured grid domains and free boundaries. Algebraic equations for the flow variables are obtained by applying the Galerkin method to derive weak forms of the scaled momentum and energy equations. These equations are discretized with respect to time via a semi-implicit Crank–Nicolson scheme, while continuity is enforced using a SIMPLER-type algorithm (Patankar 1980).

An example of a typical finite element domain consisting of $25 \times 20 = 500$ quadrilateral elements is shown in figure 4. We originally followed the approach of other researchers and employed a quadratic variance for velocity and temperature basis functions and a linear function for pressure. This worked well in all regions except the meniscus interline where thermocapillary stress and interfacial mass transport are greatest and cause substantial pressure gradients. Unless the corner elements are made sufficiently small, this abrupt change in pressure is inaccurately applied across the entire element and over-influences the velocities at adjoining nodes.

To correct this problem, higher-order interpolations in the corner and mixed-order functions in the sidewall and meniscus regions are used for P and T. This enables application of the standard first- and second-order formulations in the interior, but

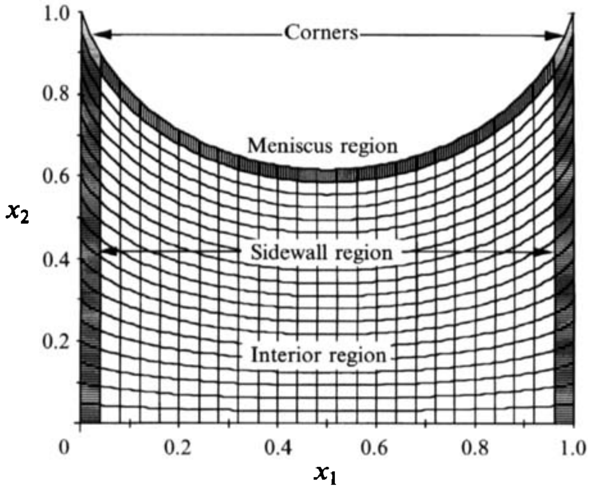

FIGURE 4. Example finite element domain consisting of 25 × 20 quadrilateral elements.

requires seven element configurations. For pressure, a quadratic approximation is applied at the two corner elements, which have a 9-node element domain and coincide with the velocity interpolation. In the interior, however, we retain a first-order variation to preserve the physical relationship between pressure and velocity. This approach requires the use of mixed-order elements. For example, the function applied along the meniscus is formulated at each of the six local nodes from the first- and second-order Lagrange polynomials. Similarly for temperature fourth- and combined fourth/second-order interpolations were used.

The first (i.e. innermost) loop in the computer model determines a velocity field that satisfies (2) based on an estimated pressure distribution. The second loop (i.e. SIMPLER algorithm) adjusts the velocity and pressure field. Once convergence is established for V_t and P, the third loop computes the temperature field. In the fourth loop, the time step is advanced to steady state, and temporal convergence is checked with the criterion that variables vary no more than 0.01 % from their previous values. In the velocity and SIMPLER loops, P is fixed at zero at the two corners at the base of the pore (i.e. lower left- and right-hand corners). By separating pressure from the stress tensor and restricting application of Green's theorem to the viscous stress tensor in the weak formulation of the momentum equation, we eliminate the need to specify pressure at the other boundary nodes.

5. Results and discussion

The problem is complicated by the fact that four dimensionless groupings, i.e. Ma, Rs, Bi and ω, are needed to define the solution. To obtain a clearer understanding of the contributions made by each convection mode, we first examine the simpler cases of conduction and single-mode convection before considering the combined thermocapillary/interfacial flow regime. Thus, we consider four cases, namely (i) the basic state or non-convective regime, (ii) pure evaporation and condensation, (iii) subcooled and superheated thermocapillary flow, and (iv) combined mode convection. To aid in the analysis, we derive three dependent parameters which characterize the key processes occurring here, namely interfacial heat and mass transfer, the flow field in the cavity and the total thermocapillary force on the meniscus. For interfacial transport, we define the thermal potential Π by

$$\Pi = \int_{\Gamma_4} T \,\mathrm{d}\Gamma_4. \tag{17}$$

This quantity is related to the total heat and mass transfer across the meniscus by $Q = Bi\Pi$ and $J = \Pi/Rs$, respectively. It is also proportional to the average temperature difference between the meniscus and bulk vapour.

The influence of interfacial temperature, contact angle and surface orientation on thermocapillary stress is characterized by the surface traction $F_i = Ma\Theta_i/Pr$, where Θ_i represents the nonlinear contribution due to Bi and ω, namely

$$\Theta_i = -Bi\int_{\Gamma_4} T\frac{g_k s_k}{g_j n_j} s_i \,\mathrm{d}\Gamma_4. \tag{18}$$

In (18) g_i is the unit vector parallel to the gradient $T_{,i}$, while $g_k s_k/g_j n_j$ is the ratio between the tangential and normal components of interfacial heat flux. Θ_i is the nonlinear contribution to the total thermocapillary force in the x_i-direction, and heat flux tangent to the surface. With heat flow normal to the surface (i.e. $g_k s_k = 0$ and $g_k n_k = 1$), $\Theta_i = 0$. Alternatively, with a completely insulated boundary ($g_k n_k = 0$), all heat at the surface flows tangentially thus yielding pure thermocapillary flow. Note that owing to the symmetry of the problem, the horizontal component Θ_1 vanishes, and only the vertical component represented by Θ_2 is non-zero when $\omega \neq 90°$.

In addition to J, the flow field is characterized by a half-cavity circulation C that arises from the angular momentum caused by inequality between velocities along the centreline and no-slip region of the sidewall, that is

$$C = \int_{\Gamma} V_i s_i \,\mathrm{d}\Gamma. \tag{19}$$

For the left half-cavity, the equation for C is integrated counterclockwise along the composite surface Γ containing the vertices $(x_1, x_2) = (0, 1), (0, 0), (0.5, 0)$ and $(0.5, y_0^{(s)})$. As we will discuss later, half-cavity circulation is useful for assessing the competition between simultaneously occurring convection modes.

5.1. *Basic state*

In the basic state, heat transfer between the pore boundaries occurs solely by conduction. Since the boundary conditions for surface velocity and thermocapillary stress are expressed as functions of T and $\partial T/\partial s$, the basic-state interfacial temperature yields insight regarding the driving mechanisms for convection within the cavity. To examine this regime, we set $V_i = 0$ and solve the steady-state diffusion equation for temperature $T_{,jj} = 0$ while applying the Robin condition in (16).

Several calculations were performed within the parameter ranges of $1 \leqslant Bi \leqslant 10^2$ and $0 \leqslant \omega \leqslant 90°$. The sensitivity of liquid temperature to Bi is illustrated in figure 5 which compares the interfacial temperature distributions corresponding to $\omega = 15°$, and $Bi = 1$, 10 and 10^2. The most obvious trend from these plots is the increase in cavity thermal gradient at larger values of Bi. As $Bi \rightarrow \infty$, conduction becomes the rate-limiting process for heat transfer, and the gradient must increase to support enhanced heat transfer between the liquid and vapour. In addition, the increased heat transfer with the vapour phase results in a lower average temperature difference between the surface and bulk vapour, that is $|T| \rightarrow 0$. This represents the state of complete

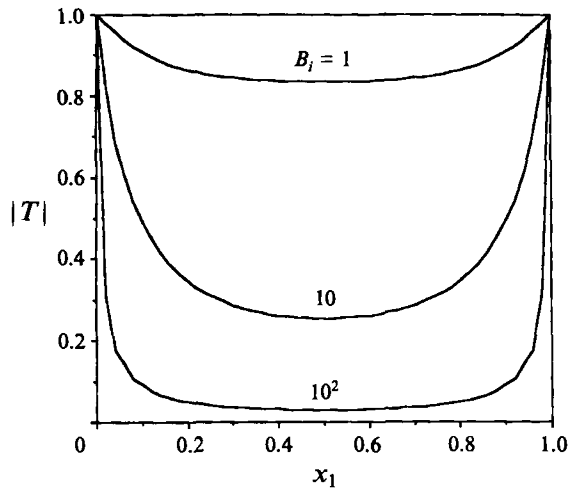

FIGURE 5. Magnitude of basic-state interfacial temperature $|T|$ versus x_1 at $\omega = 15°$.

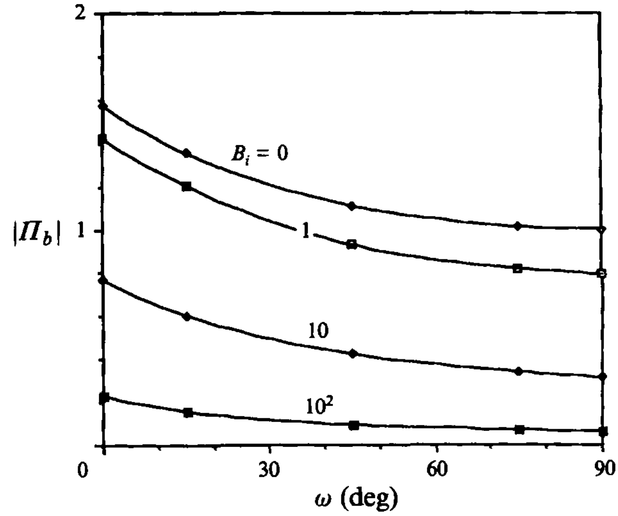

FIGURE 6. Magnitude of basic state thermal potential $|\Pi_b|$ versus ω and Bi.

equilibrium between the vapour and liquid and is consistent with the definition of Rs in that $Rs \to 0$. Alternatively, as $Bi \to 0$, the non-equilibrium limit is approached, $1/Rs \to 0$, and surface convection becomes the rate-limiting process. This reduces the liquid thermal gradient but raises the temperature difference between the liquid and vapour, $|T| \to 1$.

The overall influence of Bi and ω on heat and mass transfer is illustrated in figure 6 which shows the variation of $|\Pi|$ for the basic state (i.e. $|\Pi_b|$) over the aforementioned parameter ranges. As explained earlier, increasing Bi lowers the average temperature difference between the liquid and vapour, thereby reducing $|\Pi|$. The most significant effects of contact angle are the change in area available for heat transfer and the variation of T and thermal gradient along the surface $\partial T/\partial s$. The change in T and $\partial T/\partial s$ is less with smaller contact angles due to the surface's increase in area and steeper orientation relative to the internal temperature gradient. Since the total supportable

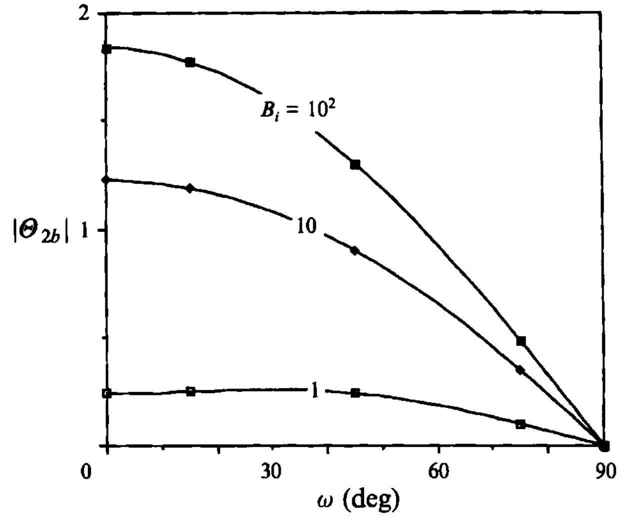

FIGURE 7. Magnitude of basic state thermocapillary force $|\Theta_{2b}|$ versus ω and Bi.

heat transfer at a given Bi becomes greater as $\omega \rightarrow 0$, preservation of the pore energy balance requires that the thermal gradient decrease and the temperature distribution become more uniform. These effects and the increase in surface area mutually contribute to raising $|\Pi_b|$ as $\omega \rightarrow 0$. This behaviour is especially evident at lower Bi, because the surface temperature becomes more uniform as it approaches the constant bulk vapour temperature.

Although fluid convection and stress are ignored, the surface temperature distributions associated with the basic state yield a $\partial T/\partial s$ which can be characterized in terms of the normalized total thermocapillary force Θ_2 (i.e. Θ_{2b}). Figure 7 shows how $|\Theta_{2b}|$ varies with Bi and ω. Reducing ω generally increases the thermocapillary force, although at $Bi = 1$, $|\Theta_{2b}|$ actually attains a small maximum at $15° < \omega < 45°$. The more important observation, however, is that the total force vanishes as $\omega \rightarrow 90°$ and the surface flattens. The sensitivity of $|\Theta_{2b}|$ to contact angle also tends to increase with larger Bi because of the concentration of temperature change near the sidewalls at this condition. In other words, a greater portion of the total thermocapillary force becomes restricted to the vertical regions of the surface as ω is lowered.

5.2. *Pure evaporation and condensation*

To model pure evaporation and condensation, the thermocapillary stress is ignored by setting $Ma = 0$. This minimizes the tangential component of surface velocity, resulting in a vertically oriented flow field. An example of the streamfunction Ψ and temperature distributions for condensation and evaporation with $Rs = 10^{-1}$, $Bi = 1$ and $\omega = 15°$ is shown in figure 8. Although no surface traction is present, a tangential component of surface velocity does exist due to curvature and the non-uniformity in temperature. This can be seen by the slight bending of the streamlines towards the sidewall near the meniscus. This directional bias arises because the temperature difference between the meniscus and vapour, which represents the driving potential for mass transport, is a maximum at the contact line. The main consequence of this phenomenon is an increase in the local vorticity near the surface and strengthening of the circulation present on either side of the cavity.

Figure 8 also indicates the typically lower flow intensities associated with

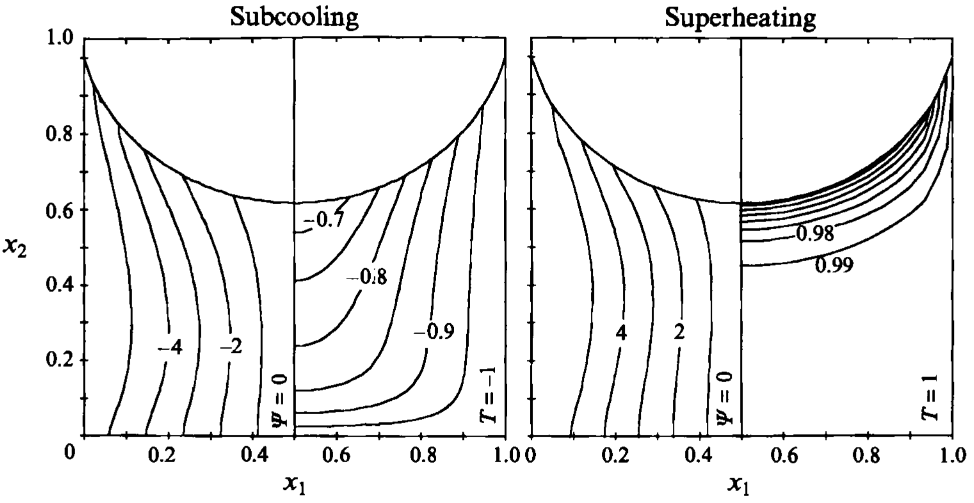

FIGURE 8. Flow field and temperature distributions for pure interfacial flow with $Rs = 10^{-1}$, $Bi = 1$ and $\omega = 15°$.

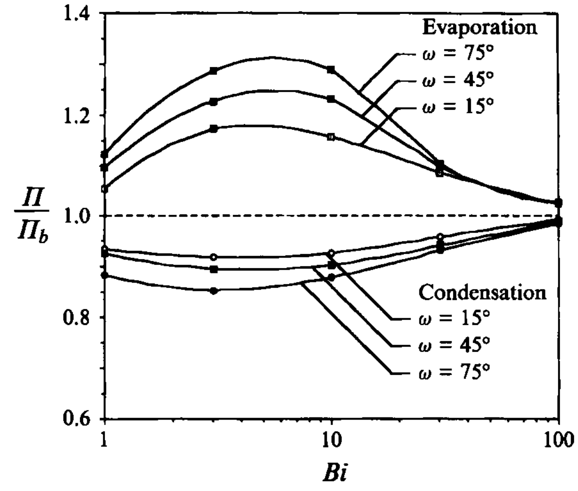

FIGURE 9. Deviation of thermal potential from basic state Π/Π_b versus Bi and ω for pure interfacial flow.

condensation. The reason for this becomes clearer upon examination of figure 9 which shows the departure of Π from the basic state via the ratio Π/Π_b. With evaporation, $\Pi/\Pi_b > 1$, which implies that the average temperature difference between the meniscus and the bulk vapour is always greater than the basic-state value. This agrees with the results of Chen *et al.* (1989) who noted the same augmenting influence of evaporation on interfacial heat and mass transfer. This tendency is due to compression of isotherms caused by the flow of superheated liquid from the bottom of the cavity which raises the temperature near the surface. With condensation, $\Pi/\Pi_b < 1$ because the downward flow distends the temperature field about the surface and compresses the isotherms towards the bottom of the cavity. The condensation of warm liquid on the surface raises the temperature, thus suppressing the driving potential for heat and mass flow into the cavity and lowering Π relative to the basic state.

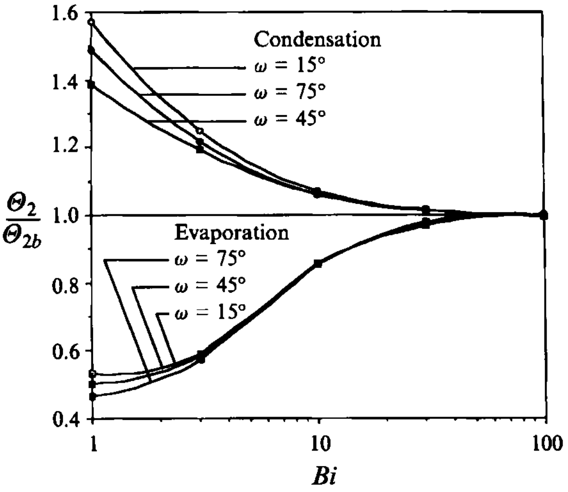

FIGURE 10. Deviation of thermocapillary force from basic state Θ_2/Θ_{2b} versus Bi and ω for pure interfacial flow.

Figure 9 also shows the dependence of Π/Π_b on Bi and ω at $Rs = 10^{-1}$. Although the sensitivity to Bi is typically stronger than that to ω, the deviation from the basic state vanishes (i.e. $\Pi/\Pi_b \rightarrow 1$) at very high and low Bi, and yields a maximum between $3 < Bi < 10$. When Bi is large, heat transfer is limited by conduction, and the interfacial and domain temperature distributions are affected less by fluid motion within the cavity. With vanishing Bi, on the other hand, the more uniform liquid temperature restricts the magnitude of temperature variation near the surface. The maximum deviation occurs at the transition between conduction- and convection-limited heat transfer processes, when fluid convection within the domain plays a key role in dictating the temperature distribution.

Evaporation and condensation also have different effects on the temperature gradient and the thermocapillary force along the surface. Figure 10 shows the ratio Θ_2/Θ_{2b} as a function of Bi and ω. The fact that $\Theta_2/\Theta_{2b} < 1$ for evaporation confirms that this mode of interfacial transport tends to reduce the average temperature gradient and cause a lower total thermocapillary force in the vertical direction than the basic state. It also suggests that evaporation may suppress the total thermocapillary force in a combined flow situation. Condensation exhibits an opposite effect on the thermocapillary force with $\Theta_2/\Theta_{2b} > 1$. As in the case of Π/Π_b, at very high and low values of Bi there is little deviation from the basic state. Although it is not shown in figure 10, the maximum deviation occurs at $Bi \approx 1$ for evaporation and lower values for condensation.

The influence of condensation and evaporation on circulation is summarized in figure 11. Although the half-cavity circulations for the two modes are opposite in sign, the differences in magnitude are very small. The most apparent trend is the higher circulation associated with small contact angles. This is due to the larger centreline velocities caused by the increase in $|\Pi|$ and exposed surface area. With large ω, the streamlines become more perpendicular to the surface and further reduce the contribution of surface velocity to circulation intensity. The importance of these trends will become apparent later when we discuss the effect of fluid flow on dynamic pressure and show that the combination of higher circulations and small contact angles promotes large interfacial pressure gradients.

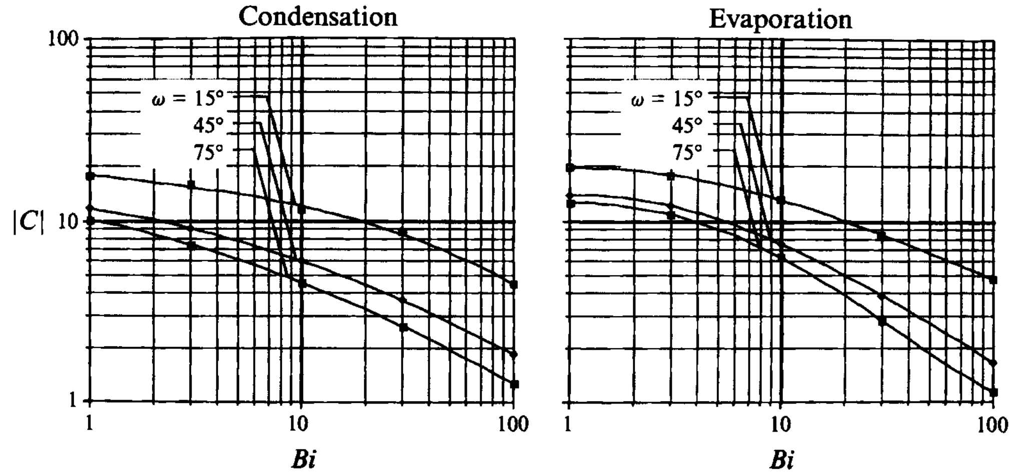

FIGURE 11. Magnitude of half-cavity circulation |C| versus *Bi* and ω for pure interfacial flow.

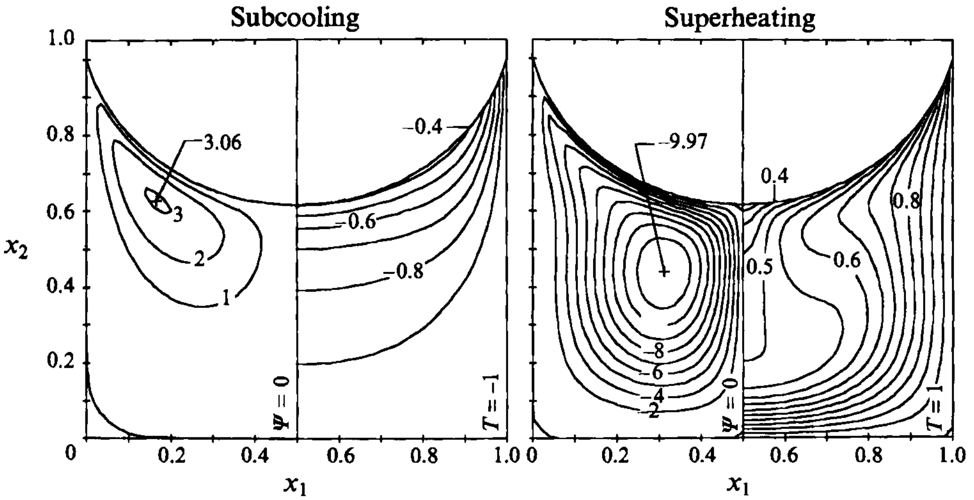

FIGURE 12. Flow field and temperature distributions for pure thermocapillary flow with $Ma = 10^3$, $Bi = 10$ and $\omega = 15°$.

5.3. *Pure thermocapillary flow*

To examine pure thermocapillary flow, the interfacial resistance is fixed at a high value ($Rs = 10^3$) to eliminate the normal component of velocity and ensure parallel flow at the surface. Figure 12 shows the steady-state Ψ- and T-distributions for a subcooled and superheated cavity with $Ma = 10^3$, $Bi = 10$ and $\omega = 15°$. For both heating modes, the thermocapillary stress, which acts opposite to the surface temperature gradient, establishes twin counter-rotating vortices symmetric about the cavity centreline. With subcooling, the meniscus temperature gradient from the centreline to the walls is negative and causes a traction towards the corners. This establishes counterclockwise and clockwise rotations in the left and right sides of the cavity, respectively. With superheated boundaries the gradient is positive and the traction on either side is directed into the centre. The senses of cell rotation for the two heating modes are opposite.

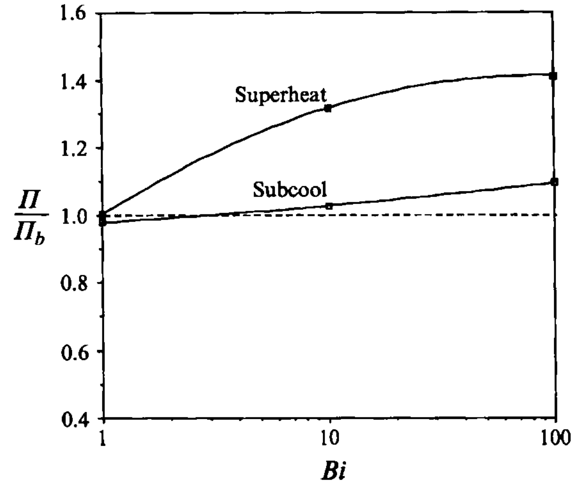

FIGURE 13. Π/Π_b versus *Bi* for pure thermocapillary flow with $Ma = 10^3$ and $\omega = 15°$.

In the case of subcooling, surface fluid convected towards the sides of the cavity deforms the isotherms away from the centreline and establishes a higher $|\partial T/\partial s|$ in the vicinity of the sidewall. Return circulation from the lower portion of each cell convects subcooled liquid upwards through the centre, thus compressing the isotherms and causing a temperature depression in the middle of the surface. With superheating, the isotherms near the surface deform into the centre of the cavity due to the transport of heated liquid from the sidewalls. This circulation, which is consistently stronger than subcooling, causes isotherm deformation in the direction of flow and a reduction of $|\partial T/\partial s|$ near the corners. The isotherms about the axis of symmetry extend down into the fluid due to the transport of cool liquid from the surface. The circulation is also evidenced by the return flow at the bottom which shifts the isotherms towards the sidewalls.

Results from other combinations of *Ma* and *Bi* indicate that superheating consistently yields a stronger circulation than subcooling. This difference is primarily due to the manner in which the circulation cells situate near regions of concentrated stress. That is, the cells shift towards the sidewall with subcooling, but move towards the centreline when superheated. The viscous losses associated with these positions are quite different. At the sidewall, subcooled flow accelerated along the surface encounters the stationary boundary at a higher relative velocity than the superheated regime, which meets it at the bottom of the cell. Thus, the viscous losses along the walls are greater for the subcooled regime. At the centreline, however, both modes experience a slip condition caused by opposing flow from the other side of the cavity. Although the viscous losses here are greater for superheating, the losses for both modes are less than those at the sidewall. Consequently, the superheated flow regime incurs less viscous losses and a higher circulation than subcooling.

The response of surface temperature to thermocapillary convection yields a more complex deviation of Π from the basic state than pure evaporation or condensation. Figure 13 shows Π/Π_b as a function of *Bi* for $Ma = 10^3$. We see that the deviation in Π for both heating modes increases with *Bi*. With superheating, hot liquid flows from the sidewalls to the centre, and from the bottom to the corners. Cellular convection in this case is complementary to the interfacial temperature gradient and tends to raise Π. This observation was also made by Chen *et al.* (1989) who noted an increase in average

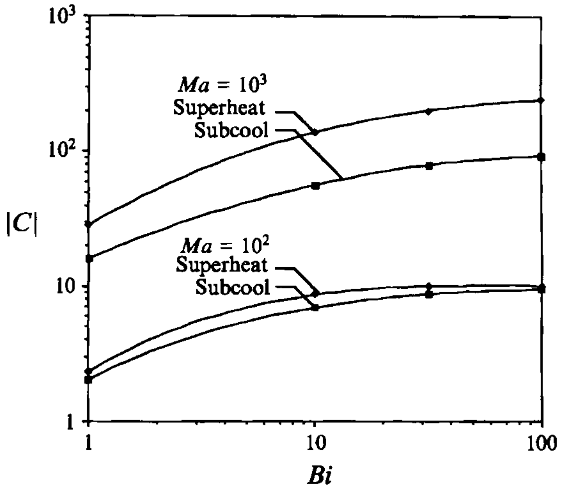

FIGURE 14. Half-cavity circulation as a function of *Bi* and *Ma* for pure thermocapillary flow and $\omega = 15°$.

interfacial temperature with larger values of *Ma* and *Bi*. With subcooling, however, the heated liquid convected along the surface tends to raise interfacial temperature and lower Π, while the upward circulation of cooler fluid causes a localized depression in the temperature profile that increases Π. This competition arises because upwelling opposes the surface temperature gradient and can cause $\partial T/\partial s$ to vary in sign between the centreline and sidewall. Although the influence of upwelling increases with *Bi*, Π/Π_b for subcooling is always less than superheating. In fact, at low *Bi* surface convection dominates the interfacial temperature profile and $\Pi/\Pi_b < 1$.

Figure 14 illustrates the variation in circulation magnitude with *Bi* for $Ma = 10^2$ and 10^3. As noted before, the circulation for superheating is consistently higher than subcooling due to the difference in viscous losses. In addition, $|C|$ tends to increase with *Bi* due to the greater temperature gradients. At low *Ma*, the values of $|C|$ for both modes converge at high and low *Bi* due to the reduced convection-driven distortion of the temperature field. As $Bi \to 0$, the more uniform surface temperature causes $\partial T/\partial s \to 0$ and $|C| \to 0$. Alternatively, as $Bi \to \infty$, the temperature field becomes conduction-limited and independent of fluid convection. These trends also apply at the higher value of *Ma* ($= 10^3$) and low *Bi* due to the vanishing circulation. At higher *Bi*, however, the surface temperature is much more sensitive to superheating and acquires a distribution that increases the thermocapillary stress force relative to subcooling. This difference in behaviour persists as $Bi \to \infty$.

To examine the influence of contact angle on the thermocapillary-driven flow field, we consider $\omega = 75°$, $45°$ and $15°$, while holding *Ma* and *Bi* constant at 10^2 and 10, respectively. Figure 15 compares the half-cavity Ψ-distributions for 75° and 15°, and clearly indicates a suppression of circulation at larger contact angles. This result seems to contradict Kamotani & Platt (1992) who noted a decrease in circulation intensity with smaller ω. The disparity is primarily due to the asymmetric heating conditions that they imposed versus the symmetric heating considered in this paper. In their problem, Θ_1 makes the principal contribution to the net thermocapillary force, while the influence of Θ_2 is negligible. Unlike the reference behaviour noted for Θ_2 in figure 7, Θ_1 for the asymmetric configuration tends to increase with larger contact angles (Schmidt 1993).

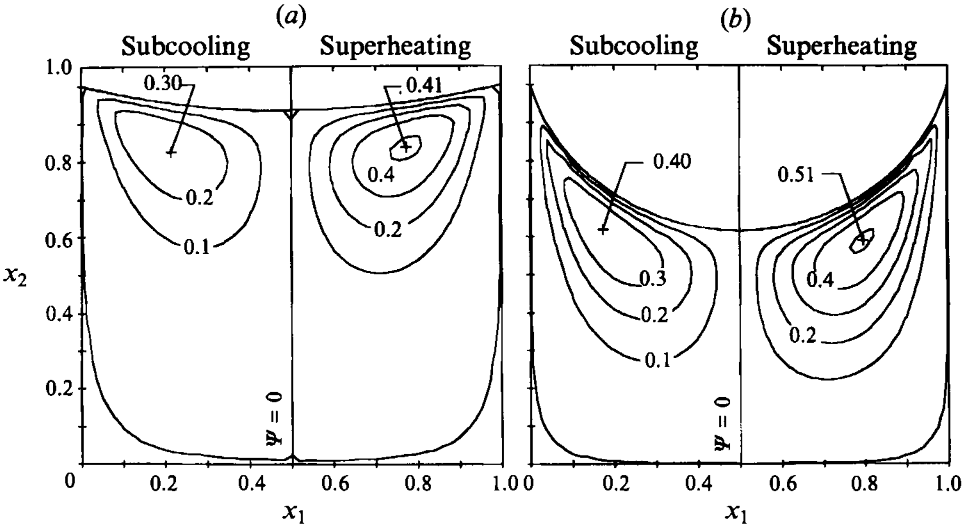

FIGURE 15. Influence of contact angle and heating mode on flow field for pure thermocapillary flow with $Ma = 10^2$, $Rs = 10^3$ and $Bi = 10$: (*a*) $\omega = 75°$, (*b*) $\omega = 15°$.

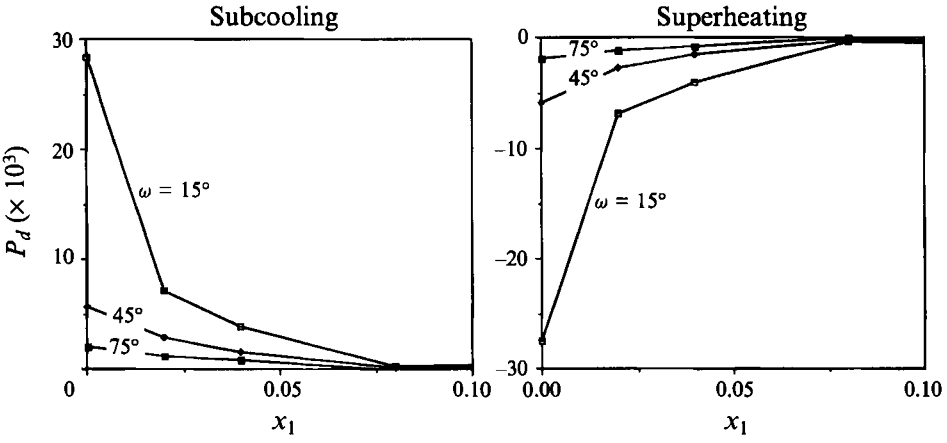

FIGURE 16. Surface dynamic pressure P at four nodes adjacent to left sidewall for pure thermocapillary flow with $Ma = 10^2$ and $Bi = 10$.

Upon comparing the circulation trends here with those for pure evaporation and condensation in figure 11, we see that the circulation magnitude arising solely from phase change has a much lower magnitude than that for thermocapillary flow. However, the magnitudes in figures 11 and 15 share the same functional dependence on ω. We will show later that this tendency provides an additive effect on parameters that depend on ω, such as the dynamic pressure gradient, in combined flow situations.

An important feature of this flow regime is the manner in which small contact angles lead to large dynamic pressure gradients near the sidewall region. This phenomenon is illustrated in figure 16 which shows pressure values at the four surface nodes adjacent to the left sidewall. With subcooling, surface flow directed towards the sidewalls causes a rise in pressure and a suction in the middle of the meniscus. With superheating, the flow is reversed towards the centreline resulting in a suction at the sidewalls. In all

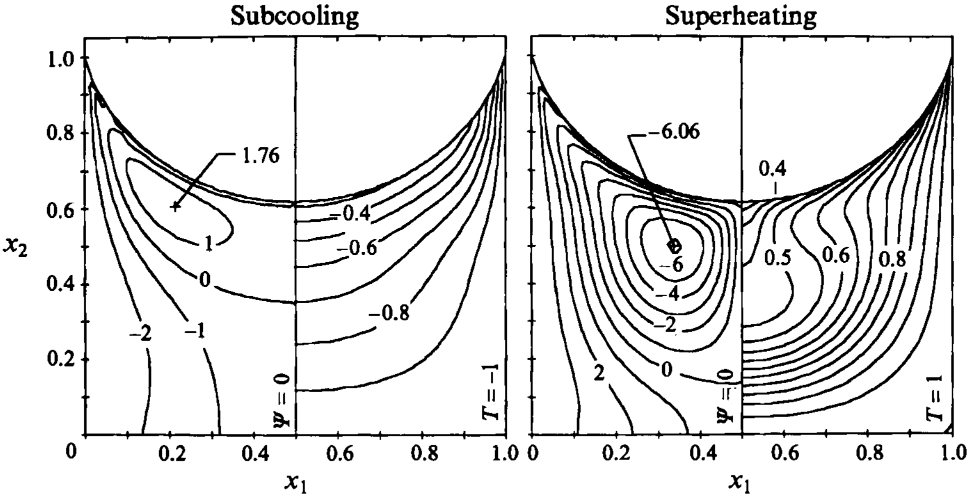

FIGURE 17. Flow field and temperature distributions for combined thermocapillary/interfacial flow with $Ma = 10^3$, $Rs = 10^{-1}$, $Bi = 10$ and $\omega = 15°$.

cases, the pressure distribution in the centre of the cavity is relatively flat, and only becomes significant at the sidewall. The chief cause of this phenomenon is the need to accommodate a large mass flow rate through an area that becomes increasingly constricted with smaller contact angles. The difference in sign (i.e. $P \ll 0$ for superheating and $P \gg 0$ for subcooling) is due to the different directions of thermocapillary stress application.

5.4. *Combined flow regimes*

Since interfacial phase change and thermocapillary yield opposing circulations when subjected to the same heating conditions, the combined regime reflects a competition between two convection modes. The relative influence of each is indicated by the half-cavity circulation C which changes sign according to the predominance of either regime.

Figure 17 shows examples of combined mode condensation and evaporation for $Ma = 10^3$, $Rs = 10^{-1}$ and $Bi = 10$. With subcooling, the flow field assumes a circulation pattern similar to its pure thermocapillary counterpart, but it also contains negative-value streamlines representing the flow of condensing liquid from the interline region to the bottom of the cavity. Unlike the pure thermocapillary case in figure 12, this flow tends to shift the vortices on either side of the cavity to the centreline, and causes a distention of surface isotherms towards the bottom, similar to its pure condensation counterpart. From the standpoint of circulation, $C = 46.45$, which is less than the value of its pure thermocapillary counterpart ($C = 56.24$). Although the combined regime seems to be thermocapillary-dominant, its $|\Pi|$ value of 0.55 is less than either the pure thermocapillary or condensation cases (which are 0.62 and 0.56, respectively). The reason for this is indicated in figure 17 by the difference between sidewall and centreline streamfunctions at $x_2 = 0$, i.e. $|\Delta\Psi|$, which reflects mass transfer through the half-cavity. For the combined regime, $|\Delta\Psi| = 2.73$, which is close to the value for pure condensation ($|\Delta\Psi| = 2.78$).

It is clear that the heat transfer for combined convection does not represent a simple superposition of thermocapillary and condensation effects. Rather, thermocapillarity modifies the surface temperature in a manner that augments the tendency of condensation to accumulate warm fluid on the surface. This behaviour is tantamount to removing the $|\Pi|$-increasing influence of upwelling in subcooled thermocapillary flow. In combined mode condensation, the cooler centre region that results from upwelling is eliminated by warm condensate in the middle of the cavity. Without this offsetting influence, the sole action of thermocapillary is to extend this warm region towards the corners, thereby lowering the thermal potential relative to pure condensation.

With superheating, the evaporation flux, which is represented by positive-value streamlines, convects the vortices and liquid towards the corners. The circulation magnitude for this case ($C = -102.31$) is lower than its pure thermocapillary counterpart ($C = -137.85$), but the flow clearly remains thermocapillary-dominant. The thermal potential for superheating remains the same as pure thermocapillary flow at $|\Pi| = 0.797$. Although the flow field is thermocapillary-dominant in terms of circulation and thermal potential, the total mass flow rate across the meniscus ($|\Delta\Psi| = 3.77$) is greater than its pure evaporation counterpart ($|\Delta\Psi| = 3.49$), and the surface temperature profile promotes evaporation.

Figure 17 clearly shows that evaporation and condensation compete with thermocapillary flow by reducing the magnitude of half-cavity circulation. However, the trends noted for $|\Delta\Psi|$ and $|\Pi|$ indicate that thermocapillarity tends to accentuate the influence of condensation and evaporation on interfacial heat/mass transfer and surface temperature.

The influence of Ma, Rs and Bi is summarized in figure 18 which shows circulation versus Rs for $Ma = 10$ and 10^2, and $Bi = 1$, 10 and 10^2. To facilitate comparisons, a corrected circulation C^* is used, where $C^* = C$ for superheating/evaporation and $C^* = -C$ for subcooling/condensation. With these definitions, thermocapillary-dominance is indicated when $C^* < 0$, while phase-change-dominance occurs when $C^* > 0$. The transition region is defined to include not only the crossover point at $C^* = 0$, but also the bounds where C^* changes from being relatively independent of Rs (i.e. $Rs > 1$) to being strongly dependent on Rs and Bi (i.e. $Rs \leqslant 10^{-1}$).

At the lower limit of Bi ($= 1$), thermocapillary flow is relatively weak compared to either condensation or evaporation. The low interfacial temperature gradient in this case yields a very low circulation intensity in the thermocapillary-dominant region. The influence of Ma in this case is vanishingly small as illustrated by the almost negligible difference in C^* between $Ma = 10$ and 10^2. For this range of Ma, the transition regime occurs between $0.5 < Rs < 10$. At lower values of Rs (i.e. $Rs < 0.1$) interfacial flow clearly dominates and dictates circulation intensity.

With superheating, the influence of Ma on C^* essentially vanishes for $Rs < 10^{-1}$, and the flow becomes solely a function of Bi and Rs. The increasing accumulation of warm liquid as $Rs \rightarrow 0$ reduces the interfacial temperature gradient and diminishes the influence of Ma. This behaviour, however, does not apply to subcooling, which assumes a lower C^* and distinct Ma-dependency for $Rs < 10^{-1}$. As discussed before, the lower C^* is due to the suppressing influence of condensation on $|\Pi|$. This reduction in $|\Pi|$ is complemented by an associated increase in Θ_2 and thermocapillary stress. Thus, the differences in Ma persist at low Rs, and tend to augment the suppression of $|\Pi|$ at larger condensation rates.

At higher Bi ($= 10$), the increased temperature gradient shifts the transition to thermocapillary dominance to lower values of Rs. In addition, the flow field and transition region are more sensitive to values of Ma. At the lower limit of Ma ($= 10$), thermocapillary flow is still relatively weak, and the transition region shifts only

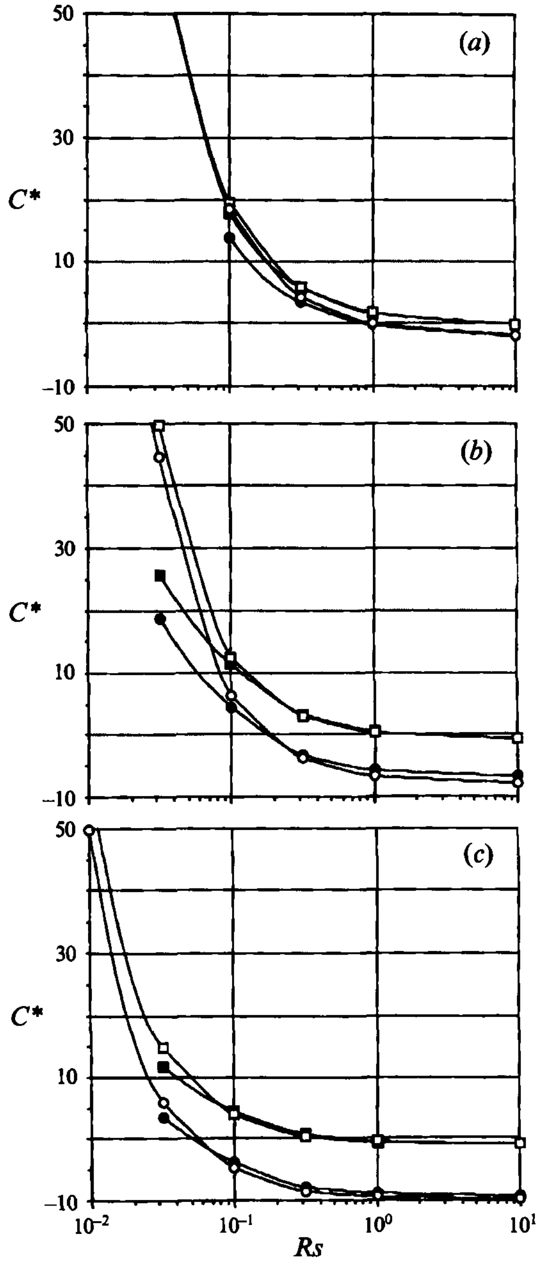

FIGURE 18. Corrected half-cavity circulation C^* versus Ma, Rs and Bi for $\omega = 15°$ and (*a*) $Bi = 1$, (*b*) $Bi = 10$, (*c*) $Bi = 10^2$. □, Superheat, $Ma = 10$; ○, superheat, $Ma = 10^2$; ■, subcool, $Ma = 10$; ●, subcool, $Ma = 10^2$.

slightly to the left. At higher Ma ($= 10^2$), however, the shift to a range of $0.03 < Rs < 0.3$ is more noticeable. Although it cannot be discerned from the plot, we expect C^* for $Ma = 10$ and 10^2 to converge as $Rs \rightarrow 0$.

We again observe the different slopes exhibited by the subcooling and superheating curves in the transition region due to the opposite influence of evaporation and condensation on interfacial temperature. With superheating and evaporation,

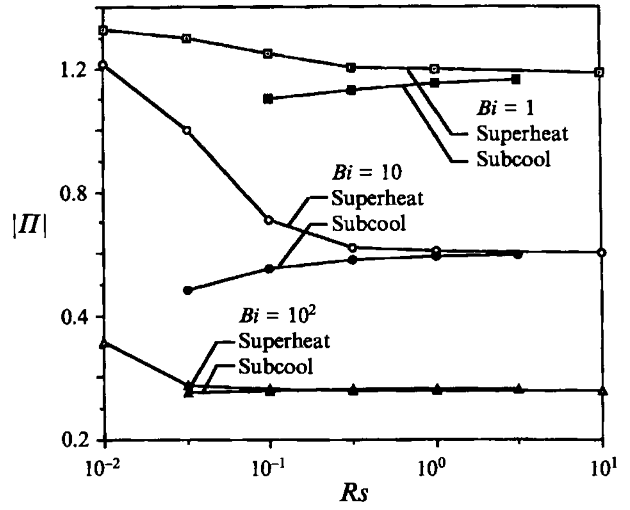

FIGURE 19. Magnitude of thermal potential $|\Pi|$ versus *Rs* and *Bi* for combined thermocapillary/interfacial flow and $\omega = 15°$.

interfacial temperature and $|\Pi|$ increase steadily with lower *Rs* due to isotherm compression. With subcooling, however, $|\Pi|$ is reduced owing to distension of isotherms towards the bottom of the cavity. The *Rs* value at which this behaviour becomes noticeable tends to decrease at higher *Bi*. At $Ma = 10^2$, the crossover point occurs near the transition $C^* = 0$. This means that over the entire range of *Rs* and *Bi*, C^* for superheating is always greater than subcooling. This is not the case at the lower limit of *Ma*. Here, it appears that there are values of *Rs* at which C^* is greater for condensation.

A further increase in *Bi* to 10^2 yields the same trends as before. Here, however, the thermocapillary influence is even greater as reflected by the clearly lower transitional ranges. The transition from thermocapillary flow at $Ma = 10$ occurs at $Rs \approx 0.5$, while at $Ma = 10^2$ it occurs at $Rs \approx 0.05$. The temperature suppression of condensation is also more evident and creates a distinct disparity in the C^* values for subcooling and superheating in the interfacially dominated flow region. With this combination of parameters it appears that the influence of thermocapillarity persists for $Rs \leqslant 10^{-2}$ since the curves do not appear to converge. However, it is expected that the convergence noted before will occur as $Rs \rightarrow 0$.

The influence of *Rs* and *Bi* on $|\Pi|$ at $Ma = 10^2$ is shown in figure 19. With superheating, both thermocapillarity and evaporation augment one another in terms of their influence on $|\Pi|$. Since the Marangoni number examined here is too small to effect appreciable distortion of the temperature field, the value of $|\Pi|$ in the thermocapillary-dominant regime ($Rs \geqslant 1$) is essentially constant and equivalent to the basic-state value in figure 6. For $Rs < 1$, however, $|\Pi|$ increases relative to the basic state due to the compression of isotherms towards the surface. We also see that the deviation in Π is greatest at a *Bi* close to 10, which is consistent with trends for pure evaporation in figure 9. With condensation, the thermal potential in the thermocapillary-dominant region still closely approximates the basic state because of the small isotherm deformation. With reduced *Rs*, however, $|\Pi|$ decreases owing to the previously noted increase in surface temperature.

Figures 18 and 19 clearly illustrate the complex interactions between thermocapillary flow and evaporation/condensation. The parameters *Ma*, *Rs* and *Bi* are useful in

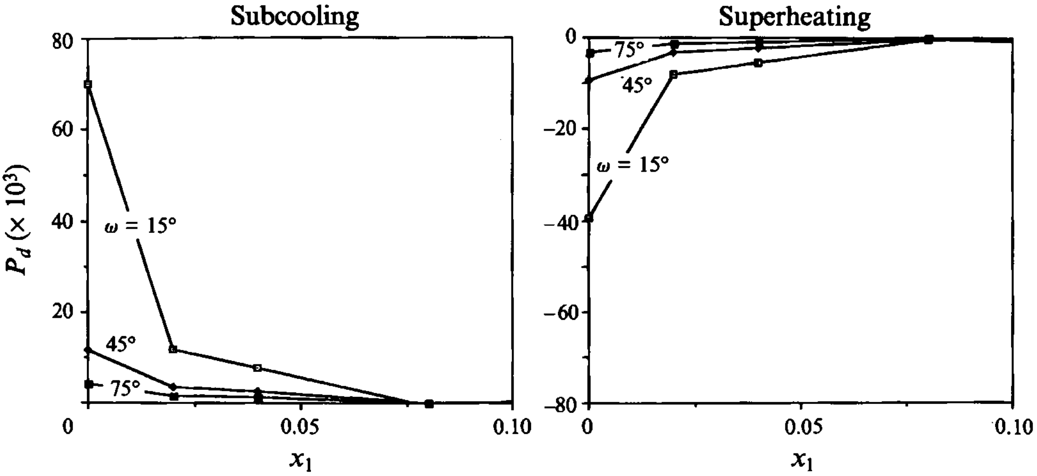

FIGURE 20. Surface dynamic pressure P at four nodes adjacent to left sidewall for pure thermocapillary flow with $Ma = 10^2$, $Rs = 10^{-1/2}$ and $Bi = 10$.

delineating the various regimes and types of interactions. High values of Ma, Rs and Bi all lead to thermocapillary dominance, while low values promote evaporation or condensation. The interactions appear to be maximized at intermediate values, such as $Ma = 10^3$, $Rs = 10^{-1}$ and $Bi = 1$ or $Ma = 10^2$, $Rs = 10^{-1/2}$ and $Bi = 10$. These cases are of interest in examining the effect of convection on surface morphology.

In figures 11 and 14 we found that small contact angles increase circulation intensity for both pure evaporation/condensation and thermocapillary flow. In addition, we showed in figure 16 that the increase in circulation with pure thermocapillary flow can lead to large dynamic pressure gradients near the meniscus contact line. We had argued in §5.3 that ω should have an even stronger effect on the flow field and lead to larger dynamic pressure gradients for the combined regime. Figure 20 shows the dynamic pressures near the sidewall for $Ma = 10^2$, $Rs = 10^{-1/2}$ and $Bi = 10$. It is likely that the meniscus could not sustain such large gradients, thus violating the assumption of fixed meniscus shape in this study. In a subsequent paper we will reconsider the retention problem while accounting for a deformable interface, and it will be shown that such excessive pressure gradients can indeed lead to large deformations of the free surface.

6. Conclusions

The influence of two-phase thermocapillary convection on the flow and thermal behaviour of a volatile wetting fluid in a small open cavity has been examined. Owing to the complexity of the problem, we first considered the effects of interfacial phase change and thermocapillarity separately before analysing their simultaneous influence. The convection associated with pure evaporation tends to raise the temperature difference between the meniscus and bulk vapour, thereby promoting interfacial transport. Condensation, however, exhibits an opposite effect due to the accumulation of warm fluid on the surface. These differences are maximized at an intermediate value of Bi of around 10. The circulation associated with both modes is comparable and tends to increase with lower values of Bi.

Both subcooled and superheated thermocapillary flow tend to raise the average temperature difference relative to the basic state. However, the increase for subcooling is less, owing to the competition between surface convection and upwelling in the centre of the pore. The magnitude of circulation produced by superheating is also greater owing to its lower viscous losses in the vicinity of the sidewall. Unlike evaporation and condensation, the circulation intensity for pure thermocapillary flow tends to increase with *Bi*.

In the combined regime, phase change and thermocapillarity compete in dictating half-cavity circulation. The transition between a thermocapillary- and interfacially dominant flow structure depends on the relative values of *Rs*, *Ma* and *Bi*. Larger values of these three parameters favour thermocapillary flow, while smaller values lead to evaporation or condensation dominance. However, the two modes augment each other's effect on heat and mass transfer across the meniscus. That is thermocapillarity tends to decrease the interfacial transport associated with condensation, but promotes it with evaporation.

The contact angle was shown to have a strong effect on the heat transfer and circulation for both heating modes. Lowering the contact angle increases the circulation for both pure evaporation/condensation and thermocapillary flow. In the combined regime, this trend is even more significant and encourages development of large dynamic pressure gradients along the meniscus near the sidewall. Such large gradients indicate that assuming a non-deforming meniscus is probably inappropriate, and may lead to mechanical non-equilibrium under some conditions.

REFERENCES

BERGMAN, T. L. & KELLER, J. R. 1988 Combined buoyancy, surface tension flow in liquid metals. *Numer. Heat Transfer* **13**, 49–63.

BERGMAN, T. L. & RAMADHYANI, S. 1986 Combined buoyancy- and thermocapillary-driven convection in open square cavities. *Numer. Heat Transfer* **9**, 441–451.

BURELBACH, J. P., BANKOFF, S. G. & DAVIS, S. H. 1988 Nonlinear stability of evaporating/condensing liquid films. *J. Fluid Mech.* **195**, 463–494.

CARPENTER, B. & HOMSY, G. M. 1989 Combined buoyant-thermocapillary flow in a cavity. *J. Fluid Mech.* **207**, 121–132.

CHEN, H., OSHIMA, K. & HINADA, M. 1989 Numerical analysis of thermocapillary and evaporating flows at low Bond Number. In *Proc. Symp. on Mechanics of Space Flight, Sagamihara, Japan, Nov. 24–25 1988*, pp. 39–53. Japan Inst. Space Astro. Sci.

CUVELIER, C. & DRIESSEN, J. M. 1986 Thermocapillary free boundaries in crystal growth. *J. Fluid Mech.* **169**, 1–26.

DURANCEAU, J. L. & BROWN, R. A. 1989 Finite element analysis of melt convection and interface morphology in earthbound and microgravity floating zones. In *Drops and Bubbles, 3rd Intl Colloq. Monterey, CA, 1988* (ed. T. G. Wang), pp. 133–134. AIP.

FU, B.-I. & OSTRACH, S. 1983 Numerical solutions of thermocapillary flows in floating zones. In *Transport Phenomena in Materials Processing*, pp. 1–9. ASME.

HADID, H. & ROUX, B. 1992 Buoyancy- and thermocapillary-driven flows in differentially heated cavities for low Prandtl number fluids. *J. Fluid Mech.* **235**, 1–36.

HYER, J., JANKOWSKI, D. & NEITZEL, G. 1991 Thermocapillary convection in a model float zone. *AIAA J. Thermo. Heat Transfer* **5**, 577–582.

JUE, T. C., RAMASWAMY, B. & AKIN, J. E. 1991 Computation of thermocapillary and buoyancy affected cavity flow using semi-implicit FEM. *Numer. Meth. Therm. Probs.* **7** (1), 402–412.

KAMOTANI, Y. & PLATT, J. 1992 Effect of free surface shape on combined thermocapillary and natural convection. *AIAA J. Thermo. Heat Transfer* **6**, 721–726.

KOBAYASHI, N. 1988 Steady convection caused by the temperature inhomogeneity in a cylindrical floating zone. *Japan J. Appl. Phys.* **27**, 20–24.

LAN, C. W. & KOU, S. 1991 Heat transfer, fluid flow and interface shapes in floating zone crystal growth. *J. Cryst. Growth* **108**, 351–366.

MIRZAMOGHADAM, A. & CATTON, I. 1988 A physical model of the evaporating meniscus. *Trans. ASME* C: *J. Heat Transfer* **110**, 201–207.

OSTRACH, S. & KAMOTANI, Y. 1992 Recent developments in oscillatory thermocapillary flows. In *Proc. AIAA/IKI Microgravity Science Symp.*, pp. 25–32. AIAA.

PALMER, H. J. 1976 The hydrodynamic stability of rapidly evaporating liquids at reduced pressure. *J. Fluid Mech.* **75**, 487–511.

PATANKAR, S. V. 1980 *Numerical Heat Transfer and Fluid Flow*. Hemisphere.

POTASH, M. & WAYNER, P. 1972 Evaporation from a two-dimensional extended meniscus. *Intl J. Heat Mass Transfer* **15**, 1851–1863.

RENK, F. J. & WAYNER, P. C. 1979 An evaporating ethanol meniscus – Part II: Analytical studies. *Trans. ASME* C: *J. Heat Transfer* **101**, 59–62.

SCHMIDT, G. R. 1993 Thermocapillary flow with evaporation and condensation and its effect on liquid retention in low-g fluid acquisition devices. PhD dissertation, The University of Alabama in Huntsville.

SCHMIDT, G. R., CHUNG, T. J. & NADARAJAH, A. 1995 Thermocapillary flow with evaporation and condensation at low gravity. Part 2. Deformable surface. *J. Fluid Mech.* **294**, 349–366.

SEN, A. K. 1986 Thermocapillary convection in a rectangular cavity with a deformable interface. *Phys. Fluids* **29**, 3881–3883.

SEN, A. K. & DAVIS, S. H. 1982 Steady thermocapillary flows in two-dimensional slots. *J. Fluid Mech.* **121**, 163–186.

SHEN, Y., NEITZEL, P., JANKOWSKI, D. & MITTELMANN, H. 1990 Energy stability of thermocapillary convection in a model of the float-zone, crystal growth process. *J. Fluid Mech.* **217**, 639–660.

STRANI, M., PIVA, R. & GRAZIANI, G. 1983 Thermocapillary convection in a rectangular cavity: asymptotic theory and numerical simulation. *J. Fluid Mech.* **130**, 347–376.

SWANSON, L. W. & HERDT, G. C. 1992 Model of the evaporating meniscus in a capillary tube. *Trans. ASME* C: *J. Heat Transfer* **114**, 434–441.

SWANSON, L. W. & PETERSON, G. P. 1994 Evaporating extended meniscus in a V-shaped channel. *AIAA J. Thermo. Heat Transfer* **8**, 172–180.

WERHLE, V. & VOULELIKAS, G. 1985 Evaporation from a two-dimensional meniscus. *AIAA J.* **23**, 309–313.

ZEBIB, A., HOMSY, G. M. & MEIBURG, E. 1985 High Marangoni number convection in a square cavity. *Phys. Fluids* **28**, 3467–3476.